Scattering and Roughness Analysis of Indoor Materials at Frequencies from 750 GHz to 1.1 THz

Fawad Sheikh, Yamen Zantah, Ismail Ben Mabrouk, *Senior Member, IEEE*, Mai Alissa, Jan Barowski, *Member, IEEE*, Ilona Rolfes, *Member, IEEE*, and Thomas Kaiser, *Senior Member, IEEE*

***Abstract*—The problem of wave propagation and scattering at terahertz (THz) frequencies has become increasingly important, in particular for accurate modeling of future indoor wireless communication channels. The reflective properties of indoor materials with different surface roughness and dielectric constants are important to explore diffuse scattering for accurate channel modeling. First and foremost, a THz *Swissto12* system is adopted to obtain the first ever transmission measurements for a wide choice of indoor material groups such as *wood, plastic* and *brick* at frequencies from 750 GHz to 1.1 THz using up-conversion (frequency-domain) method. Both the reflection (S_{11}, S_{22}) and transmission coefficients (S_{12}, S_{21}) are measured using this novel and non-invasive electromagnetic technique. The inversion method based on Kramers-Kronig (K-K) relations is then applied to convert the calibrated scatter data into intrinsic material properties (i.e., refractive index, permittivity, absorption coefficient). Then, the surface topography of rough material samples is acquired using surface measurement instruments. Further, the optically smooth ($\sigma_h/\lambda \ll 1$) materials are assorted as most to least rough based on Rayleigh roughness factor. Lastly, the ray tracer considering the Rayleigh-Rice (R-R) scattering model is employed to obtain the maximum achievable reflected paths of the above mentioned indoor material samples at 300 GHz followed by their experimental validation.**

***Index Terms*—THz, Swissto12 MCK, vector network analyzer, material characterization, indoor rough materials, ray tracing.**

I. Introduction

FACT that many radio scientists around the globe are interested in THz regime (0.3–4 THz) for wireless communications owes to the available overwhelming extreme wide bandwidths that are explicitly attractive for terabit-per-second (Tb/s) wireless applications [1]–[5]. Some of the most anticipated promising 5G applications such as 8K 360 degree videos, vehicle-to-everything (V2X) bidirectional communications, and augmented/mixed reality may require in the near future wireless data transmission capacity beyond 100 Gb/s. In fact, public WiFi hotspots serving users with such high-speeds and bandwidth-intensive wireless applications also tend to deal with the rapid explosion of wireless data traffic in the coming years. More devices than ever are making matters worse. In addition, the present industrial automation is relying on cables due to the limited range and mobility of the current WiFi data transmission capacity. In other words, it can therefore be said that the present-day wireless networks fall nowhere near to the "wireless everything" or "everything wireless" era. In this work, *wireless* refers to the point-to-point radio systems that propagate inside rooms. Nonetheless, a number of novel applications for high speed data links such as 5G cellular network, terabit wireless local area networks (T-WLANs), terabit wireless personal area networks (T-WPANs), cloud servers and ultrafast kiosk downloads are realizable by taking the advantage of THz frequencies thus cutting the cord to go fully wireless progressing into the "Tera-Era".

The 100 Gb/s barrier crossover by wireless means incites numerous "real world" applications not only in wireless communications but also in material characterization which is of great interest to the researchers in spectroscopy, imaging, sensing, screening, and many more. Therefore, characterization of indoor material dielectric properties at these frequencies is of paramount importance. It needs to be accomplished with high precision through appropriate measurement and extraction techniques. The material intrinsic properties (i.e., complex refractive index etc.) are so far extensively investigated at lower frequencies, however published information for applications within the THz frequency spectrum region of interest is still limited.

Formerly, only THz time-domain spectroscopy (THz-TDS) system based on down-conversion (time-domain) method has been applied to measure the intrinsic responses of the materials [6]–[9]. This work specifically reports the first ever measurements for a wide choice of indoor material groups such as *wood, plastic* and *brick* at frequencies from 750 GHz to 1.1 THz using up-conversion (frequency-domain) method employing *Swissto12* material characterization kit (MCK) waveguide system [10] in transmission geometry. At THz frequencies, the common indoor building materials have high reflection and transmission losses [11]. The VNA-based waveguide measurement techniques in transmission mode are the most favorable since the transmission loss in the reflection mode increases as the incident angle to the material is increased further increasing the path length inside the material. The measured S-parameters are converted to complex dielectric properties to obtain frequency dependent refractive index and

F. Sheikh is with the Institute of Digital Signal Processing, University of Duisburg-Essen, Germany e-mail: fawad.sheikh@uni-due.de.

Y. Zantah is with the Institute of Digital Signal Processing, University of Duisburg-Essen, Germany e-mail: yamen.zantah@uni-due.de.

I. Mabrouk is with School of Engineering and Computer Sciences, Durham University, Durham, UK e-mail: ismail.benmabrouk@durham.ac.uk.

M. Alissa is with the Institute of Digital Signal Processing, University of Duisburg-Essen, Germany e-mail: mai.alissa@uni-due.de.

J. Barowki is with the Institute of Microwave Systems, Ruhr-University Bochum, Germany e-mail: jan.barowski@rub.de.

I. Rolfes is with the Institute of of Microwave Systems, Ruhr-University Bochum, Germany e-mail: ilona.rolfes@rub.de.

T. Kaiser is with the Institute of Digital Signal Processing, University of Duisburg-Essen, Germany e-mail: thomas.kaiser@uni-due.de.

absorption coefficient using the inversion method based on Kramers-Kronig (K-K) relations [12].

The paper is structured as follows. The THz reflection models along with Rayleigh roughness factor are introduced in Section II. Then, the 9 material samples are concisely presented in Section III. This section is further enhanced by describing the two surface measurement tools and the (VNA-based) *Swissto12* MCK THz transmission waveguide measurements system operating at frequencies from 750 GHz to 1.1 THz. Next, Section IV presents the results and discussions under one umbrella based on the analysis. Section V is exclusively dedicated to the ray tracing simulations conducted at 300 GHz for the chosen 9 material samples prior to the conclusions in Section VI.

II. THz Reflection Models

A. Fresnel Reflection Model

At THz frequencies, the characteristics of the reflection in case of ideally smooth and homogeneous surfaces such as *A*1, *A*3 and *B*2 (*cf.* Table I) can be described by the well known Fresnel reflection coefficient Γ [13]. The Fresnel reflection coefficient expressions for perpendicular (Γ_{TE}) and parallel (Γ_{TM}) polarizations for such smooth surfaces are expressed in [14, p. 21] as

$$\Gamma_{\mathrm{TE}}(f,\Theta_i) = \frac{Z\cos\Theta_i - Z_0\cos\Theta_t}{Z\cos\Theta_i + Z_0\cos\Theta_t} \tag{1}$$

and

$$\Gamma_{\mathrm{TM}}(f,\Theta_i) = \frac{Z\cos\Theta_t - Z_0\cos\Theta_i}{Z\cos\Theta_t + Z_0\cos\Theta_i} \tag{2}$$

Here, Θ_i is the incident angle, $\Theta_t = \arcsin(\sin(\Theta_i)Z/Z_0)$ is the angle of refraction, $Z_0(=377\ \Omega)$ denotes the free space impedance and Z being the wave impedance of the reflecting material is calculated as

$$Z = \sqrt{\frac{\mu_o}{\varepsilon_o\left(n^2 - \left(\frac{\alpha c}{4\pi f}\right)^2 - \mathrm{j}\frac{2n\alpha c}{4\pi f}\right)}} \tag{3}$$

where μ_o, ε_o, c, and f are free space permeability, permittivity, velocity, and the frequency of the incident wave, respectively. α is the absorption coefficient and n is the frequency dependent refractive index of the material samples. The complex refractive indices of the materials are obtained from the method based on K-K relations [12]. From the imaginary part of the complex refractive index, the absorption coefficient of a material can be obtained [15].

B. Rayleigh-Rice Reflection Model

At lower frequencies, the surface of indoor materials is principally regarded as a smooth surface. However, as the frequency rises into the lower end of THz spectrum (i.e., 300 GHz), the wavelength is so short that it is quite close or even on the order of the surface roughness of optically smooth indoor materials. The optically smooth materials are not ideally smooth since an ideally smooth surface is defined as one for which the standard deviations of surface height σ_h is always

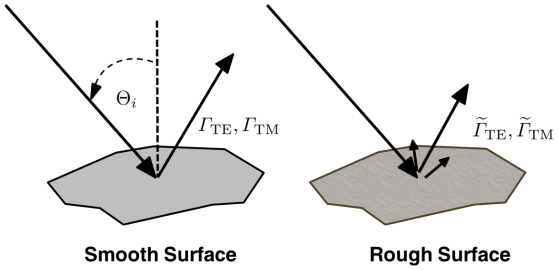

Fig. 1: Illustration of specular reflection by a smooth surface (left) and diffuse reflections by a rough surface (right).

equal to zero regardless of the frequency range. Hence, the term optically smooth implies to the indoor materials which at lower frequencies behave like ideally smooth materials but at THz frequencies the $\sigma_h \neq 0$ mm for these optically smooth surfaces and the scattering phenomenon is thus more likely to occur. Therefore, in the THz range we can no longer regard every indoor material surface as smooth and must therefore expect the rough surface scattering phenomenon [16]. These scattering losses cause a decrease in the reflected power in the specular direction [17]. In fact, the reflected power in the specular direction from a rough surface is lower than that from a smooth surface as shown qualitatively in Fig. 1. In other words, the modified reflection coefficient $\widetilde{\Gamma}$ should be smaller than the conventional Fresnel reflection coefficient Γ in case of rough surface.

In THz range, the Fresnel reflection coefficients are to be multiplied by the Rayleigh roughness factor to account for the decrease in reflected energy in specular direction due to the slight roughness in these materials [13]. Thus, the scattering losses for the specular reflections are equal to the Rayleigh roughness factor (ρ_{spec}) expressed in [14, p. 81] as

$$\rho_{\mathrm{spec}} = e^{-\frac{g}{2}} = \exp\left(-\frac{8\pi^2\, f^2\, \sigma_h^2\, \cos^2\Theta_i}{c^2}\right), \quad \rho_{\mathrm{spec}} \in [0,1] \tag{4}$$

where g from [14, p. 82] is

$$g = \sigma_h^2(2\pi f/c)^2(\cos(\Theta_i))^2 \tag{5}$$

or

$$g = k^2\sigma_h^2(\cos(\Theta_i) + (\cos(\Theta_r))^2$$

Here, g is the roughness parameter of a material, f the frequency of incident wave, σ_h the standard deviation height of surface roughness, Θ_i the angle of incidence and reflection relative to surface normal, and c the velocity of light. Note that for the setup in our study depicting a transmission geometry ($\Theta_i = \Theta_r = 0°$), we have

$$\Gamma_{\mathrm{TE}} = \Gamma_{\mathrm{TM}} \tag{6}$$

Furthermore, the expression in Eq. (6) applies also for very small incident angle ($\Theta_i \approx 0°$). The modified reflection coefficients $\widetilde{\Gamma}$ in the presence of rough surfaces (e.g., *W*1, *W*2, *W*3, *W*4, *W*5, and *B*3) taking into account the different standard deviation heights are then expressed as

$$\widetilde{\Gamma}(f,\Theta_i) = \rho_{\mathrm{spec}}\,\Gamma(f,\Theta_i) \tag{7}$$

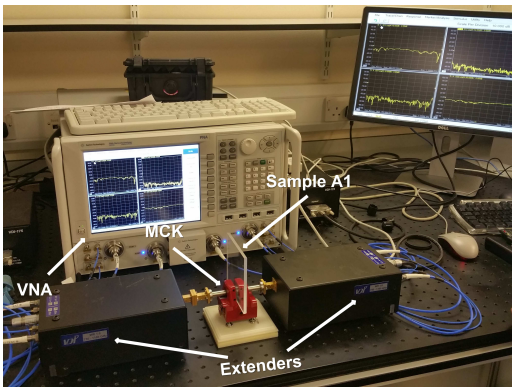

(a) MCK *Swissto12* System

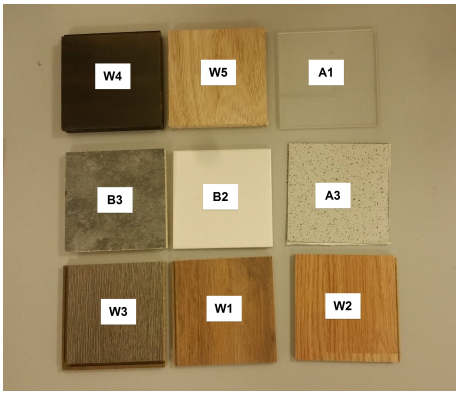

(b) Material Samples

Fig. 2: The 750 GHz to 1.1 THz VNA system at University of Glasgow.

From Eq. (7), it is apparent that $\widetilde{\Gamma}(f,\Theta_i)$ is always smaller than $\Gamma(f,\Theta_i)$. It is noteworthy to mention that for materials which are optically smooth, the conventional reflection coefficients Γ do conform with the measurements for longer wavelengths (i.e., at lower frequencies) but deviate for shorter wavelengths (i.e., at THz frequencies). This is due to the roughness of the optically smooth indoor materials that become evidently rough at THz frequencies and thus scatter. Consequently, this entails the channel models with surface roughness at THz frequencies [18] and the novel scattering algorithms [19]. Thus, in [13] this deviation is rectified by including the Rayleigh roughness factor.

Once $\Gamma(f,\Theta_i)$ and $\widetilde{\Gamma}(f,\Theta_i)$ are determined, then rearrangement of Eq. (7) evaluates the Rayleigh roughness factor ρ_{spec} as

$$\rho_{\text{spec}}(f,\Theta_i,\sigma_h) = \frac{\widetilde{\Gamma}(f,\Theta_i)}{\Gamma(f,\Theta_i)} \tag{8}$$

III. Material Samples and Roughness Characterization

A. Description of Material Samples

We characterized three indoor building material groups such as *wood*, *plastic* and *brick* encountered in the indoor wireless propagation channel. The knowledge of the thicknesses of material samples is mandatory in extracting the material parameters and hence, the thicknesses of different indoor materials is measured at five different locations and the average for each material sample is then tabulated in Table I.

TABLE I: LIST OF MEASURED MATERIALS WITH THEIR THICKNESS

Mat. group	ID	Sample	Thickn.
Wood	W1**	HDF[1] (Thick)	7.5 mm
	W2**	HDF[1] (Thin)	5.5 mm
	W3**	HDF[1] (Underlay wood fibre)	12 mm
	W4**	Bamboo (hard wood)	14 mm
	W5**	Natural wood	10.5 mm
Plastic	A1*	Glass-look cast acrylic	4.75 mm
	A3*	Vinyl tile sheet	1.2 mm
Brick	B2*	White ceramic wall tile	6.5 mm
	B3**	Brown ceramic wall tile	9.7 mm

* smooth surface
** rough surface
[1] HDF: High-Density Fiberboard

B. Measurement Instruments for Surface Roughness

The knowledge of the surface topography of rough material samples used in this study is inevitable for accurately analyzing the channel performance and the limitations of THz communication systems. Whilst various indoor materials with different roughnesses are conceivable but a single instrument or measurement technique may not be sufficient for this purpose. Hence, two commercially available instruments namely, Profilometer XP-Plus 200 Stylus [20] and Confocal Microscope μsurf custom [21] based on the confocal-multi-pinhole (CMP), are employed to obtain the statistical information of the surface structure as well as surface profile. For instance, in case of the material sample brick (B3), the profilometer is incapable of measuring due to its sensitive stylus head tip which tends to get damaged upon recurrent movements on such rough surfaces with sharp peaks and deep valleys. Similarly, the confocal microscope is not of much use when the considered material sample for measurement is big. A short description of the functional principle of these instruments is given below.

Profilometer XP-Plus 200 Stylus*:* This is a computerized, high sensitivity surface profiler that measures roughness, waviness, and step height in a variety of applications. It possesses the ability to measure precision step heights from under 10 angstroms to as large as 1.2 mm. The apparatus comprises of a stylus tip that moves horizontally and vertically on the sample surface for variable lengths preset by the user. This stylus tip is further connected to a transducer which signals these vertical and horizontal movements to an analog to digital converter (ADC). The ADC then transcripts it into digital data which can be processed by the respective computer software such as MatLab for final results. The profilometer comes with its limitations such as a 50 mm x 50 mm material sample requires approximately 5 hours for measurement only. The device

calibration requires almost 15 minutes which thus makes the whole measurement process quite time consuming. However, an added benefit is its capability to measure material samples with maximum of 30 mm thickness and 55 mm scanning length.

μsurf Confocal Microscope*:* The μsurf sensor technology is based on the CMP technology. This equipment has the ability to acquire within seconds the topography, roughness and thickness of a material in the micro and nanometer (*nm*) ranges. The NanoFocus confocal microscope comes with an LED light source, a rotating multi-pinhole disc (MPD), an objective lens with a piezo drive and a charge-coupled device (CCD) camera. The LED source is focused through the MPD and the objective lens on to the sample surface. The light is reflected and reduced by the pinhole of the MPD to that part which is in focus and this is directed to the the CCD camera. In contrast to a conventional optical microscope's image that contains both sharp and blurred details, the confocal microscope's image is a capture of the unfocused blurred details. This gives it the leverage to capture high resolution in the nanometer range. Each confocal image represents a horizontal segment through the sample surface. The images are captured at different heights thus producing a stack of these within a few seconds. This image stack is then processed through the respective software to obtain the exact three dimensional height of the sample surface. An important feature of this device is its ability to characterize sample surfaces without contact, being a plus feature in case of sensitive surfaces.

A concise description of the measurement procedure with the roughness values for the different materials obtained from these instruments is presented later in Section IV-B.

C. Material Characterization Kit Swissto12

The potential of modern THz systems in material characterization offers a unique solution in imaging, sensing, spectroscopy and communication. The academia as well as industry are meanwhile contemplating as to how this emerging THz field can be implemented in a variety of "real world" applications by sharing their experimental database with the world, ranging from the dielectric properties of materials [22], to material surface textures [23] and the molecular spectroscopic database [24].

The experimental system for the THz transmission measurements in this study comprises of three parts, vector network analyzer (VNA), the *Swissto12* MCK waveguide system, and two frequency extension modules for measuring different indoor materials in the frequency range 750 GHz to 1.1 THz as shown in Fig. 2(a). The chosen THz frequencies are produced by the VNA using the extension modules and the output signal then traverses through a rectangular waveguide. The interconnecting gap between the rectangular frequency extension module waveguide and MCK's corrugated waveguide is bridged by a corrugated conical horn antenna at the narrow aperture transiting from a circular to rectangular waveguide. The purpose for this transitional waveguide design is to accomplish the THz transmission in an enclosed environment with

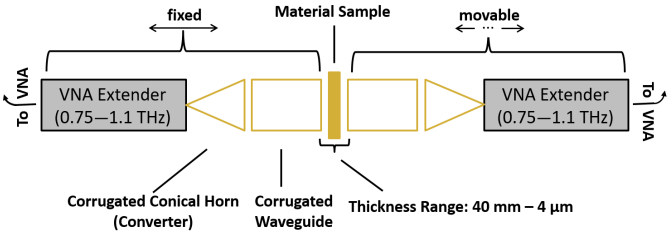

Fig. 3: Schematic diagram of *Swissto12 MCK*.

minimal losses. The transitional horn or corrugated converter more clearly depicted in the schematic layout in Fig. 3 is connected to the rectangular waveguide with adjustable flanges which are of standard size for the VNA extenders accommodating a compatible design for the waveguide converter components. Furthermore, the left hand segment of the setup is fixed as opposed to the movable right one for the ease of characterizing material samples shown in Fig. 2(b) with different thicknesses. Two-port short, open, load, and through (SOLT) WR-01 waveguide standards are acquired to calibrate the measurement equipment. This calibration streamlines the systematic errors between VNA transceivers and waveguide flanges. As the indoor materials are not chemically pure, we have selected two locations and recorded three readings for each at laboratory temperature $18^{\circ}\mathrm{C} \pm 0.2^{\circ}\mathrm{C}$ with humidity $30\% \pm 2\%$. The obtained measurement readings are then averaged for further work.

IV. Measurement Results And Discussions

A. Measured Scattering Parameters

The measured S_{21} and S_{11} of material groups namely, *wood*, *plastic* and *brick* at frequencies from 750 GHz to 1.1 THz are illustrated in Fig. 4. The fact that the values of S_{21} for all three groups are quite low indicates the high losses during transmission. These materials can thus be regarded as high-loss materials. Perhaps, the transmission attenuation, thickness of the sample as well as its permittivity, surface scattering, and absorption in the material samples result in these losses. The S_{21} values for all materials under test (MUTs) indicate considerable variation. For instance, the S_{21} values for $W1$, $W2$, $W3$, $W4$, and $W5$ at 1 THz are -52.09 dB, -49.08 dB, -48.51 dB, -48.95 dB, and -48.62 dB, respectively. Similarly, for $B2$ and $B3$ the corresponding S_{21} values at 1 THz are -49.6 dB and -46.77 dB. Lastly, for $A1$ and $A3$ these S_{21} values at 1 THz are -40.4 dB and -24.65 dB, respectively. Meanwhile, an 8.2 dB difference between S_{21} values for materials $A1$ and $A3$ is conspicuous in Fig. 4(b) at 750 GHz. The recorded data reveals that the S_{21} values are not only influenced by the thickness but the texture or inner structure of any material may also impact these values. It is also noteworthy to mention here that the thickness may influence the scattering parameters but indeed causes no impact on the intrinsic properties of any material.

The variation in S_{11} also exhibits an eminent frequency dependence being a function of the thickness of the sample as well as its permittivity. However, the recurrent big dip at

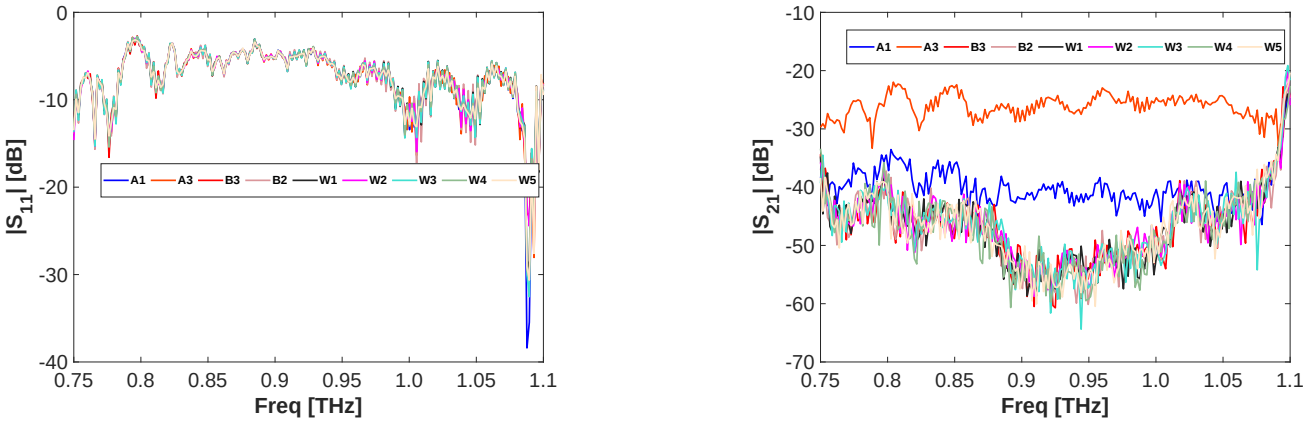

(a) S_{11} (b) S_{21}

Fig. 4: Measured S-parameters versus frequency of indoor materials using MCK system *(Material Groups: Wood, Plastic and Brick)*.

1.08 THz in S_{11} for all MUTs is likely attributed to errors and discrepancies in the measurement process, i.e., owes to the standing waves.

B. Roughness Analysis

In Table II the average roughness σ_h for each of the 6 rough materials is tabulated. The profilometer is employed for measuring the roughness of *W*3 and *W*4 samples. In case of profilometer, the sample is firstly placed on the X-Y stage. The measurement parameters such as speed, length, profile type, range, direction, stylus force and filter level are set as desired. The stylus is then moved to a desirable measuring point on the sample. The output of the profilometer measurements is in *.xml* format. These multiple output files are then processed using MatLab thus generating a 3D matrix (*x*, *y*, *z*) to acquire the surface 3D map and the height histogram of the sample surface. The height histogram is used to display the height distribution of the matrix *z* data. Finally, the mean value of the *z* data is post-processed in MatLab to calculate the standard deviation of height σ_h.

The μsurf confocal microscope is used to obtain the roughness values for *W*1, *W*2, *W*5, and *B*3. Confocal microscopy makes possible the study of the 3D surface structures at sub micron level. The sample is initially placed on an X/Y measurement table. The objective lens is vertically moved via a *z*-positioning unit which allows the acquisition of multiple digital images at different heights resulting in an image stack. Further, the output stacks of these *.nms* format files is post processed using μsurf software to generate a 3D model representing the sample surface in true height coordinates (*x*, *y*, *z*). Each individual pixel in this 3D model refers to the surface height and the measured height values for each of these result in a precise 3D reconstruction of the surface. In addition, a 2D view is also obtained with a table of roughness parameters measured in *nm* allowing different types of filters to be applied for segregating the roughness and waviness components from the primary surface. As the confocal microscopy system measures maximum up to a field size of 7.4 mm x 7.4 mm, the stitching feature of the device is utilized to analyze large samples thereby combining individual measurements carried out at different positions. A Gaussian filter with 2 mm correlation length is applied by the μsurf software when measuring the four samples at 5 different positions. Finally, the average of these measurements is then employed to calculate σ_h.

The roughness values are shown (*cf.* Table II) with the typical scanned length set in measurements for the respective material samples. The results from surface roughness measurement instruments thus assort the material samples from most to least rough in this order, i.e., *B3*, *W2*, *W1*, *W5*, *W3* and *W4*.

TABLE II: THE MEASURED STANDARD DEVIATION HEIGHTS

Material Sample	Scanned Length	σ_h
W1[a]	7.4 mm x 7.4 mm	0.0468 mm
W2[a]	7.4 mm x 7.4 mm	0.0503 mm
W3[b]	50 mm (1D)	0.0115 mm
W4[b]	50 mm (1D)	0.0111 mm
W5[a]	3.07 mm x 1.59 mm	0.0122 mm
B3[a]	7.4 mm x 7.4 mm	0.0950 mm

[a] μsurf Confocal Microscope
[b] Profilometer XP-Plus 200 Stylus

C. Rayleigh Roughness Factor

In Fig. 5, the Rayleigh roughness factor ρ_{spec} illustrates the impact of scattering and surface roughness on the 6 rough material samples versus frequency. The measured modified reflection coefficient is divided by the conventional reflection coefficient to obtain the Rayleigh roughness factor (*cf.* Eq. (8)). One is most likely able to extract a general rule from Eq. (4) that the Rayleigh roughness factor decreases with the relative increase in surface roughness, as is well evident from Fig. 5. Perhaps, the decrease in ρ_{spec} is only due to the impact of surface roughness as the angle of incidence is fixed, i.e., $\cos(0^\circ) = 1$, and thus causes no influence. It is evident that the material sample *W4* is amongst the least rough whereas *B3* is the most rough material. Upon

averaging over the frequencies, the Rayleigh roughness factor thus assorts the material samples from most to least rough in a similar order thus exhibiting a good agreement with the results obtained from the surface measurement tools. A point worthy of notice in the comparison between these two is that the Rayleigh roughness factor approach enables one to observe the frequency influence (*cf.* Fig. 5) on the material characterization. In contrast, the lateral and vertical scan resolutions from the surface measurement tools are the most important characterization parameters for surface roughness measurements (i.e., σ_h) and not the carrier frequencies.

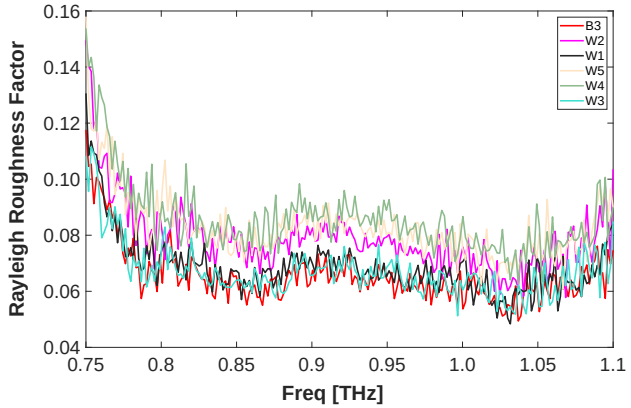

Fig. 5: Calculated Rayleigh roughness parameter ρ_{spec} versus frequency for six rough materials at angle of incidence 0° (i.e., transmission geometry).

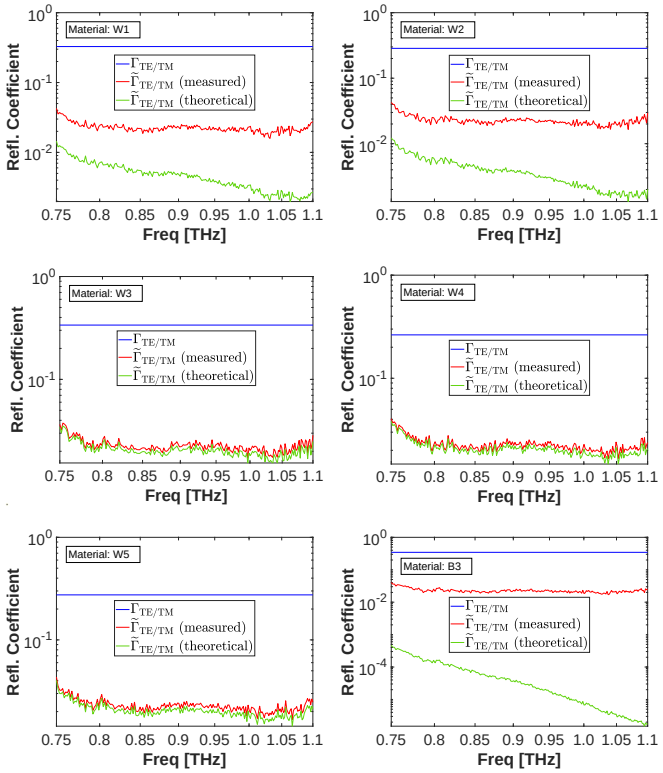

Fig. 6: Magnitude of conventional, theoretical and measured modified reflection coefficients for angle of incidence 0° versus frequency for TE/TM polarized wave *(Materials: Rough)*.

D. Reflection Coefficients

Fig. 6 plots the theoretical (green line) and measured (red line) modified reflection coefficients $\widetilde{\Gamma}$ in transmission geometry for the rough materials in our study such as $W1$, $W2$, $W3$, $W4$, $W5$, and $B3$. Here, the theoretical modified reflection coefficients are obtained using Eq. (7). The σ_h for each material taken from Table II is inserted in Eq. (4) to obtain ρ_{spec}. The conventional Fresnel reflection coefficients Γ excluding the influence of roughness are also shown in Fig. 6 as benchmark.

The constant blue line in Fig. 6 for all materials highlights the ideal behaviour of Fresnel reflection coefficient in case of lossless materials. Generally, the Fresnel reflection and transmission coefficients are well-described for the two idealized materials namely, perfect dielectrics [25] and perfect electric conductor [26]. The red curves in Fig. 6 for all materials depicting the influence from the increase in frequency express indeed good agreement with the measured modified reflection coefficients beyond 750 GHz as reported in the literature [13]. In short, Fig. 6 dominantly narrates the impact of the electrical properties (i.e., permittivity) on the conventional Fresnel reflection coefficients. The comparatively significant impact of roughness in case of both theoretical and measured modified reflection coefficients is also visible in this figure. Another point worthy of mention is that the aforementioned observation in our study applies when angle of incident $\Theta_i = 0°$.

V. Ray Tracing Simulations

The THz regime is indubitably among today's candidates with a huge potential to explore veiled applications in wireless communications with centimeters to hundreds of meters in range. Earlier experiments [2], [27]– [29] have been limited to desktop scenario of up to one meter relying on line-of-sight (LoS) conditions. In our previous experiment [1], the line-of-sight channel measurements have been presented in the frequency range (300–310) GHz at 5 m distance. Nevertheless, the aforementioned studies are not conducted in NLoS scenarios. The knowledge of the reflected paths with maximum path lengths imperative for defining both the use-cases and real world applications is thus lacking. To the best of the authors knowledge, no such works exist which target this imperative knowledge for either the aforementioned or any other indoor materials.

Abiding by the already approved IEEE 802.15.3d-2017 Standards, the carrier frequency f_c of interest in our study is 300 GHz unlike the chosen frequency range for measurements (i.e., 750 GHz - 1.1 THz). The 300 GHz measurements were opted keeping in account the restricted dynamic range of the WM-250 (WR-1.0) extenders with the peak dynamic range of 94 dB at 10 Hz intermediate frequency (IF) bandwidth. A spectral window within this carrier frequency offers 47 GHz of continuous bandwidth with low atmospheric attenuation which allows a 100 Gb/s high throughput even with a simple modulation scheme. Also, at f = 300 GHz (spectral window)

TABLE III: MEASURED PARAMETERS OF MATERIALS USED IN RAY-TRACING

Mat. group	ID	$\tilde{\epsilon}_r$	$\tilde{\tilde{\epsilon}}_r$	σ_h	Thickn.
Wood	W1	3.88	0.192	0.0468 mm	7.5 mm
	W2	3.23	0.10	0.0503 mm	5.5 mm
	W3	4.06	0.152	0.0115 mm	12 mm
	W4	2.86	0.474	0.0111 mm	14 mm
	W5	3.08	0.123	0.0122 mm	10.5 mm
Plastic	A1	2.64	0.0190	0.0000 mm	4.75 mm
	A3	2.4	0.0340	0.0000 mm	1.2 mm
Brick	B2	4.0	0.0820	0.0000 mm	6.5 mm
	B3	4.20	0.10	0.0950 mm	9.7 mm

the atmospheric attenuation for both LoS and NLoS cases is identical and as low as 0.1 dB [30].

A. Link Budget Analysis

At 300 GHz, using the Friis formula to determine the received power at the transceiver in our realistic VNA-based channel measurement system gives

$$P_{\mathrm{RX}}(d, f_c) = P_{\mathrm{TX}} + G^{\mathrm{TX}} + G^{\mathrm{RX}} - \mathrm{PL}(d, f_c) \tag{9}$$

Here, *transmit power* P_{TX} equal to -10 dBm represents the test port power or a baseband signal power from the R&S ZVA67 VNA. The R&S ZC330 converter (i.e., a frequency extension module) acting as a transceiver contains frequency multipliers to transform the VNA's port RF signal into our target frequency range. G^{TX} and G^{RX} are the gains for transmitter and receiver antennas, respectively. At 300 GHz, these gains are equal to 25.45 dBi and can be doubled to obtain the total gain due to use of horn antenna as the transceiver. $\mathrm{PL}(d, f)$ is the path loss which collectively represents $\mathrm{L_F}$ being the free space path loss (FSPL), atmospheric attenuation loss $\alpha(f_c)$, and the miscellaneous losses X_m further including transmitter conversion losses $\mathrm{L_{TX}}$, depolarization losses due to surface scattering $\mathrm{L_{DP}}$, reflection losses from MUT $\mathrm{L_{RL}}$, and losses from receiver $\mathrm{L_{RX}}$. With d being the path length from horn antenna as transceiver (i.e., TX) to reflection point (i.e., MUT) and then further from reflection point to transceiver (i.e., RX). Thence, the path loss in 300 GHz is expressed as

$$\mathrm{PL}(d, f_c) = \mathrm{L_F} + (\alpha(f_c)\, d) + X_m \tag{10}$$

or

$$\mathrm{PL}(d, f_c) = 20 \log\left(\frac{\lambda_c}{4\pi d}\right) + (\alpha(f_c)\, d) + \mathrm{L_{TX}} + \mathrm{L_{DP}} + \mathrm{L_{RL}} + \mathrm{L_{RX}} \tag{11}$$

where λ_c is the wavelength at hand. It is worth pointing out that the $\mathrm{L_{DP}}$ here represents the change in polarization of the incident wave due to surface scattering from a rough surface and not geometrical depolarization. Because reflection by a rough surface is not only scattering the field towards non-specular directions but also depolarizing it. Likewise, the 300 GHz measurement equipment is calibrated as such to minimize the $\mathrm{L_{TX}}$ and $\mathrm{L_{RX}}$ to no more than 1 dB. Finally, Eq. (9) is rewritten to give the received power as

$$P_{\mathrm{RX}}(d, f_c) = P_{\mathrm{TX}} + G^{\mathrm{TX}} + G^{\mathrm{RX}} - 20 \log\left(\frac{\lambda_c}{4\pi d}\right) - (\alpha(f_c)\, d) - \mathrm{L_{TX}} - \mathrm{L_{DP}} - \mathrm{L_{RL}} - \mathrm{L_{RX}} \tag{12}$$

B. Simulated Environment Scenario

The path loss is required in order to calculate the received power (*cf.* Eq. 9). The simulations thus conducted enabled us to obtain this for the chosen 9 material samples. The simulation results for two of these material samples namely, $W2$ and $A1$ are then experimentally validated. These measurements are conducted at f_c = 300 GHz using a 25.45 dBi horn antenna transceiver based VNA measurement setup. Unlike simulations, the MUTs employed for the validation measurements are 1.5 m in dimensions. The horn from measurement setup is designed using CST MWS [31] and the 3D radiation pattern at 300 GHz is then exported for ray tracer simulations. The simulated environment is modeled as a reflection scenario comprised of an empty seminar room BB1204 in our Institute of Digital Signal Processing (DSV). This seminar room layout is 10 m (*length*) x 5.3 m (*width*) x 5 m (*height*) in dimensions as shown in Fig. 7.

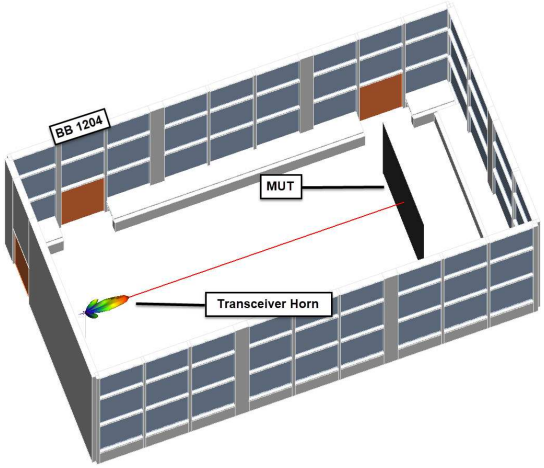

Fig. 7: Simulated realistic seminar room BB1204 environment with CST designed 3D radiation pattern from horn antenna.

In the simulation setup, the transceiver horn at a height of 1.5 m is placed at a distance of 7.2 m from the MUTs. This separation distance is the most suited in the given setup particularly chosen keeping in account the measurement setup and to achieve the reflected paths with maximum path lengths. As the transceiver simultaneously acts as a transmitter and receiver, a reflection of 14.4 m is thus achieved and the FSPL in this case is 105.1 dB. The first Fresnel zone radius is 4.24 cm and the beam forming distance (far field) begins at 12.8 cm for the chosen 300 GHz frequency. The MUTs considered for the simulations are identical in dimensions being 3 m with different thicknesses tabulated in Table III. This Table also presents the electrical parameters measured using FMCW radar system in [32] but with a THz source of 250 GHz. These measured electrical parameters at 250 GHz are considered

TABLE IV: RELATIVE RECEIVED POWER FOR REFLECTED PATH FROM MATERIAL SAMPLES

Material Sample	Simulated PL [dB]	Simulated $P_{RX/TX}$ [dB]	Measured $P_{RX/TX}$ [dB]	X_m[dB]
R	105.38	-64.48	-63.18	–
W1	111.59	-70.69	–	6.21
W2	115.89	-74.99	-74.96	10.51
W3	110.17	-69.27	–	4.79
W4	112.26	-71.36	–	6.88
W5	113.83	-72.93	–	8.45
A1	112.40	-71.5	-70.39	7.02
A3	115.05	-74.15	–	9.67
B2	119.79	-78.89	–	14.41
B3	118.75	-77.85	–	13.37

constant at the carrier frequency of interest (300 GHz) as well affirmed by [6].

The horn antenna transceiver is vertically polarized with an average half-power beam-width of around 8° and 10° in H-plane and E-plane, respectively. Based on this employed high gain horn antenna, the beam spot size at the 7.2 m separation distance is 1.2 m in diameter and thus well within the MUT dimensions. The beam spot diameter holds a pivotal position in the THz communications and certainly deserves an in-depth investigation.

C. Simulation Results

In Table IV we present the results of our simulations and measurements. An overview of the relative received power, path loss, and miscellaneous losses for the reflected path from the 9 MUTs each is given. In addition, the metal-plate reflector denoted as *R* is employed to validate both the results and assess the miscellaneous losses (i.e., reflection and depolarization losses etc.). The measured relative received power ($P_{RX/TX}$) for the metal-plate *R* is higher than expected as evident from the simulation results. Perhaps, this is due to the preset value by the ray tracer for this idealized material.

An observable fact upon reviewing the smooth materials (*A*1, *A*3 and *B*2) is that unlike rough materials the absorption and transmission attenuation is the causative factor in this case and not surface scattering. According to the electrical parameter (i.e., complex permittivity), it is apparent that *A*1 is more reflective as compared to *A*3. Meanwhile, the transmission coefficients S_{21} (*cf.* Fig. 4b) for both *A*1 and *A*3 reveal that the transmission attenuation is more in case of *A*1 owing to its thickness as compared to *A*3. However, the miscellaneous losses (see Table IV) in case of *A*1 and *A*3 are 7.02 dB and 9.67 dB, respectively. It is noteworthy to mention that in case of smooth materials X_m represents mainly the reflection losses L_{RL}. This concludes that the L_{RL} are comparatively more in *A*3. The smooth material *B*2 manifests as the most reflective considering the electrical parameters and most lossy attributing to its thickness and transmission attenuation apparent from S_{21} (*cf.* Fig. 4b). Moreover, Fig. 8 further elaborates the Table IV by illustrating the reflection losses from the 9 MUTs at 300 GHz for different incident angles.

Next, we employed R-R model in case of the 6 rough materials which considers attenuation only in the specular

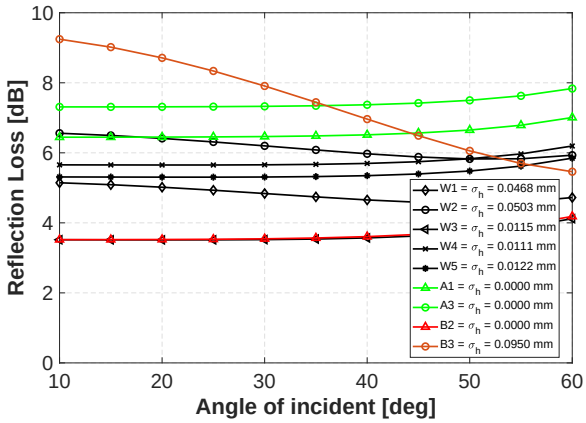

Fig. 8: Reflection losses from combined Fresnel at 300 GHz for different incident angles for materials listed in Table III.

direction of reflection. The X_m mainly comprises of the L_{RL} and L_{DP} losses. As can be acquired from the results, *B*3 is most reflective (i.e., $\tilde{\epsilon}_r$ = 4.20) but also most lossy (i.e., X_m = 13.37 dB) among the rough materials. This is mainly due to the impact of roughness affirming that the surface roughness costs far more reflection loss than its electrical properties do [14, p. 5]. However, it should be noted that *B*2 is comparatively less thick than *B*3 but exhibits more transmission attenuation (*cf.* Fig. 4b). Further, *W*3 is the least rough and also least lossy among the rough materials. Upon further comparison, *W*5 is more reflective than *W*4 but less than *W*2 which is comparatively more lossy due to its highest roughness among these three MUTs. Lastly, in case of *B*3, *W*2 and *W*1, the depolarization losses are predominantly attributive to their comparatively high roughness among all materials. To sum up, the first-order reflected paths in case of smooth materials are expected to arrive 7.02 dB, 9.67 dB, and 14.41 dB below the direct path (line-of-sight path) for *A*1, *A*2 and *B*2, respectively. Likewise, in case of rough materials these first-order reflected paths arrive 6.21 dB, 10.51 dB, 4.79 dB, 6.88 dB, 8.45 dB and 13.37 dB below the direct path (line-of-sight path) for *W*1, *W*2, *W*3, *W*4, *W*5 and *B*3, respectively.

VI. Conclusion

This paper introduces a new approach within optically s-mooth indoor materials to assort these from most to least rough

based on the Rayleigh roughness factor. The THz *Swissto12* System is employed in transmission geometry for measuring the S-parameters in the frequency range 750 GHz to 1.1 THz. It is evident from the S-parameters that all investigated indoor material groups are considered to be high-loss materials at THz frequencies. In addition, the indoor materials are less reflective at THz frequencies due to high scattering losses. Considering the Rayleigh roughness factor, the material sample *W4* is assorted as the least rough whereas *B3* is the most rough material in our study. This assortment is in agreement with the results obtained from surface measurement instruments. Our study accumulates though only few material groups but these results may act as a stimulus in future for the anticipated applications in THz wireless communications and material characterization. The beam spot diameter from high gain horn antenna with beam divergence holds a pivotal position for channel modeling in THz communications. We, thus vision a thorough quantitative investigation on its implications in our future research for other material groups as well.

Acknowledgment

The research work presented in this paper is funded by the German Research Foundation (Deutsche Forschungsgemeinschaft - DFG) Project ID 287022738 TRR 196. In addition, we thank Dr. Qammer Abbasi for providing the MCK *Swissto12* System used in our experiments at James Watt Nanofabrication Centre. Finally, we thank the outstanding anonymous Reviewers for the precious efforts and comments, a great help in improving this manuscript.

References

[1] Y. Zantah, F. Sheikh, A. Abbas, M. Alissa, and T. Kaiser, "Channel Measurements in Lecture Room Environment at 300 GHz", *2019 Second International Workshop on Mobile Terahertz Systems (IWMTS)*, pp. 1–5, Jul. 2019.

[2] A. Ghwaji, F. Sheikh, T. Schultze, I. Willms, and T. Kaiser, "Preliminary Analysis of Candle Flame Impact on THz Electromagnetic Wave Propagation", *2019 Second International Workshop on Mobile Terahertz Systems (IWMTS)*, pp. 1–5, Jul. 2019.

[3] J. Ma et al., "Channel performance for indoor and outdoor terahertz wireless links", *APL Photonics*, vol. 3, no. 5, pp. 1–12, Feb. 2018.

[4] J. Ma et al., "Security and eavesdropping in terahertz wireless links", *Nature*, vol. 563, no. 7729, pp. 89–93, Oct. 2018.

[5] T. S. Rappaport et al., "Wireless Communications and Applications Above 100 GHz: Opportunities and Challenges for 6G and Beyond", *IEEE Access*, vol. 7, pp. 78729–78757, Jun. 2019.

[6] R. Piesiewicz et al., "Properties of Building and Plastic Materials in the THz Range", *International Journal of Infrared and Millimeter Waves*, vol. 28, no. 5, pp. 363–371, Mar. 2007.

[7] J. Barowski, M. Zimmermanns, and I. Rolfes, "Millimeter-Wave Characterization of Dielectric Materials Using Calibrated FMCW Transceivers", *IEEE Transactions on Microwave Theory and Techniques*, vol. 66, no. 8, pp. 3683–3689, Aug. 2018.

[8] C. Brenner et al., "Compact diode-laser-based system for continuous-wave and quasi-time-domain terahertz spectroscopy", *Optics Express*, vol. 25, no. 11, pp. 3859–3861, Dec. 2010.

[9] R. Kohlhaas et al., "Terahertz quasi time-domain spectroscopy based on telecom technology for 1550 nm", *Optics letters*, vol. 25, no. 11, pp. 12851–12859, May 2017.

[10] Swissto12 SA, "Swissto12 MCK," *Online*, Available: http://www.swissto12.com, accessed in March 2021.

[11] J. Kokkoniemi, J. Lehtomki, V. Petrov, D. Moltchanov, and M. Juntti "Frequency domain penetration loss in the terahertz", *2016 Global Symposium on Millimeter Waves (GSMM) & ESA Workshop on Millimetre-Wave Technology and Applications*, pp. 1–4, Jun. 2016.

[12] V. Lucarini, J. Saarinen, K. Peiponen, and E. Vartiainen, "Kramers-Kronig Relations in Optical Materials Research", *SSOS*, volume 110, Apr. 2005.

[13] R. Piesiewicz et al., "Scattering Analysis for the Modeling of THz Communication Systems", in *IEEE Transactions on Antennas and Propagation*, vol. 55, no. 11, pp. 3002–3009, Nov. 2007.

[14] Petr Beckmann and Andre Spizzichino, "The Scattering of Electromagnetic Waves from Rough Surfaces", *Artech House Radar Library*, USA, 1963.

[15] D. Lee et al., "Highly Sensitive and Selective Sugar Detection by Terahertz Nano-Antennas", *Scientific reports*, vol. 5, 15459, Oct. 2015.

[16] C. Jansen et al., "Diffuse Scattering From Rough Surfaces in THz Communication Channels", in *IEEE Transactions on Terahertz Science and Technology*, vol. 1, no. 2, pp. 462–472, Nov. 2011.

[17] F. Sheikh, Y. Gao, and T. Kaiser, "A Study of Diffuse Scattering in Massive MIMO Channels at Terahertz Frequencies", in *IEEE Transactions on Antennas and Propagation*, vol. 68, no. 2, pp. 997–1008, Feb. 2020.

[18] F. Sheikh, "Novel Aspects in Terahertz: Channel Measurements, Modeling and Material Characterization", *Ph.D. dissertation*, Fachg. DSV, Univ. Duisburg-Essen, Duisburg, Germany, 2019.

[19] F. Sheikh, D. Lessy, and T. Kaiser, "A Novel Ray-Tracing Algorithm for Non-specular Diffuse Scattered Rays at Terahertz Frequencies", *in 2018 First International Workshop on Mobile Terahertz Systems (IWMTS)*, pp. 1–6, Jul. 2018.

[20] Ambios Technology, Inc, "XP-Plus Series of High Performance Stylus Profilometers, Operator's Manual", *Online*, Available: https://www.cenimat.fct.unl.pt, accessed in March 2021.

[21] NanoFocus AG, "Operation Manual μsurf custom confocal microscope", *Online*, Available: https://www.nanofocus.com/, accessed in March 2021.

[22] (2021) THz BRIDGE Spectral Database. [Online]. Available: http://www.frascati.enea.it/THz-BRIDGE/database/spectra/searchdb.htm

[23] (2021) Columbia-Utrecht Reflectance and Texture Database (CUReT). [Online]. Available: http://www.cs.columbia.edu/CAVE/software/curet

[24] (2021) High-resolution Transmission Molecular Absorption Database (HITRAN). [Online]. Available: https://hitran.org

[25] J. A. Stratton, "Electromagnetic Theory", in *McGraw-Hill*, 1941.

[26] C. A. Balanis, "Advanced Engineering Electromagnetics", in *2nd ed., Wiley*, 2012.

[27] S. Priebe et al., " Channel and Propagation Measurements at 300 GHz", *IEEE Transactions on Antennas and Propagation*, vol. 59, no. 5, pp. 1688–1698, May 2011.

[28] A. Ekti et al., "Statistical Modeling of Propagation Channels for Terahertz Band", *arXiv:1707.09740 [cs, math]*, Jul. 2017.

[29] S. Kim and A. Zajic, "Statistical Characterization of 300-GHz Propagation on a Desktop", *IEEE Transactions on Vehicular Technology*, vol. 64, no. 8, pp. 3330–3338, Aug. 2015.

[30] F. Sheikh, M. Al-Hasan, and T. Kaiser, "Novel Aspects in Terahertz Wireless Communications", in *Antennas and Propagation for 5G and Beyond*, (Telecommunications, 2020), Institution of Engineering and Technology, Chap. 12, pp. 335–378.

[31] Y. Zantah, M. Alissa, T. Kreul and T. Kaiser, "Ultra-wideband Multipath Channel Characterization at 300 GHz", in *WSA 2020; 24th International ITG Workshop on Smart Antennas*, pp. 1–5, Feb. 2020.

[32] N. Pohl, T. Jaeschke and K. Aufinger, "An Ultra-Wideband 80 GHz FMCW Radar System Using a SiGe Bipolar Transceiver Chip Stabilized by a Fractional-N PLL Synthesizer", *IEEE Transactions on Microwave Theory and Techniques*, vol. 60, no. 3, pp. 757–765, Mar. 2012.

This article has been accepted for publication in a future issue of this journal, but has not been fully edited. Content may change prior to final publication. Citation information: DOI 10.1109/TAP.2021.3076577, IEEE Transactions on Antennas and Propagation

Fawad Sheikh received the M.Sc. degree in Computer Science and Communication Engineering in 2017, and the Dr.-Ing. degree in 2019 from the University of Duisburg-Essen, Duisburg, Germany. He is currently Postdoctoral researcher at the Institute of Digital Signal Processing (DSV). From 2006 to 2011, he worked for Fraunhofer IMS, KlickTel AG, Vodafone D2 GmbH and Deutsche Telekom AG, respectively, for cellular and IT service management projects. From January 2012 to May 2017, he has been with the DSV at the University of Duisburg-Essen for the project "Wireless 100 Gb/s and beyond". Since June 2017, he is working on the project mobile MAteRIal TranscEiver (MARIE). His current research interests include systems and components in THz band communication, measurement and modeling of mobile radio channels, massive MIMO systems, and mobile material characterization and localization, within the frequency range of 250 GHz to 4 THz. He is also the Internal Coordinator of the IEEE International Workshop Series on Mobile Terahertz Systems started in 2018 and CEO of The Mobile THz Company UG, offering concept designs and performance analyses of Mobile THz Systems.

Yamen Zantah (S19) received the B.Sc. degree in electronic and communication engineering from Al-Baath University, Syria, in 2011, and the M.Sc. degree in embedded systems engineering from the University of DuisburgEssen, in 2019. From 2012 to 2014, he was the Head of the Communication Team, SADCOP, Syria. He is currently pursuing Ph.D degree with the Institute of Digital Signal Processing, University of DuisburgEssen, where he is involved in multiple research projects. His research interests include full-duplex, massive MIMO, antenna selection, channel sounding measurement systems and modeling for millimeter-waves (mmWave) and terahertz (THz) channels.

Ismail Ben Mabrouk (SM 19) received the B.A.Sc. and M.A.Sc. degrees in Electrical Engineering from the University of Lille, Lille, France in 2006 and 2007, respectively and the Ph.D. in Electrical Engineering from University of Quebec, Canada, in 2012. From 2007 to 2009 he was with Huawei Technologies, Paris, France. In 2012, he joined the Wireless Devices and Systems (WiDeS) group at University of Southern California, Los Angeles, USA. He is a recipient of the Abu Dhabi Award for Research Excellence (AARE). He is currently an Assistant Professor at Durham University, Durham, UK. His research activities have been centred on antenna design at the millimiter-wave and THz frequencies, propagation studies for Multiple-Input and Multiple-Output (MIMO) systems, Deep Learning, and Wireless Body Area Network for medical applications.

Mai Alissa obtained a Master degree in Advanced Optical Technologies, with a main major 'Optics in Telecommunication' from Friedrich-Alexander-Universitt Erlangen-Nrnberg, Erlangen, Germany, in 2016, and a Bachelor degree in Electronics and Communications Engineering from Damascus University, Syria, in 2011. Mai joined DSV in January 2017, and worked in different national and European projects, her current research focuses on indoor channel simulation and measurements, and Terahertz in communications.

Jan Barowski (S'12 - M'18) was born in Bochum, Germany in 1988. He received the B. Sc. and M. Sc. in electrical engineering from Ruhr-University Bochum, Bochum, Germany, in 2010 and 2012, respectively. Since 2012 he is with the Institute of Microwave Systems, headed by Ilona Rolfes, Ruhr-University Bochum, as a Research Assistant. In 2017 he received the Dr.-Ing. degree in electrical engineering from Ruhr-University Bochum and is now working as post-doctoral Research Scientist at the Institute of Microwave Systems. His currents fields of research are concerned with radar signal processing, radar imaging and material characterization techniques.

Ilona Rolfes (M'06) received the Dipl.-Ing. and Dr.-Ing. degrees in electrical engineering from Ruhr-University Bochum, Bochum, Germany, in 1997 and 2002, respectively. From 1997 to 2005, she was with the High Frequency Measurements Research Group, Ruhr-University Bochum, as a Research Assistant. From 2005 to 2009, she was a Junior Professor with the Department of Electrical Engineering, Leibniz Universitaet Hannover, Hannover, Germany, where she became the Head of the Institute of Radiofrequency and Microwave Engineering in 2006. Since 2010, she has led the Institute of Microwave Systems, Ruhr-University Bochum. Her fields of research concern high-frequency measurement methods for vector network analysis, material characterization, noise characterization of microwave devices, sensor principles for radar systems, and wireless solutions for communication systems.

Thomas Kaiser (M98-SM04) received the Diploma degree in electrical engineering from Ruhr-University Bochum, Bochum, Germany, in 1991 and the Ph.D. (with distinction) and German Habilitation degrees in electrical engineering from Gerhard Mercator University, Duisburg, Germany in 1995 and 2000, respectively. From 1995 to 1996, he spent a research leave with the University of Southern California, Los Angeles, which was grant-aided by the German Academic Exchange Service. From April 2000 to March 2001, he was the Head of the Department of Communication Systems, Gerhard Mercator University, and from April 2001 to March 2002, he was the Head of the Department of Wireless Chips and Systems, Fraunhofer Institute of Microelectronic Circuits and Systems, Duisburg. From April 2002 to July 2006, he was Co-Leader of the Smart Antenna Research Team, University of Duisburg-Essen, Duisburg. In the summer of 2005, he joined the Smart Antenna Research Group at Stanford University and in the winter of 2007, he joined the Department of Electrical Engineering at Princeton University, both as a Visiting Professor. From 2006 to 2011, he headed the Institute of Communication Technology at Leibniz University of Hannover, Germany. Currently, he heads the Institute of Digital Signal Processing at the University of Duisburg-Essen, is founder of three start-up companies and CEO of ID4us GmbH, an RFID centric company. He is the author and co-author of more than 300 papers in international journals and conference proceedings and two books entitled "Ultra Wideband Systems With MIMO (Wiley, 2010)" and "Digital Signal Processing for Passive RFID (Wiley, 2015)" and he is the speaker of the Collaborative Research Center "Mobile Material Characterization and Localization by Electromagnetic Sensing" (MARIE). Dr. Kaiser was the founding Editor-in-Chief of the e-letter of the IEEE Signal Processing Society and the General Chair of the IEEE International Conference on UltraWideBand in 2008, the International Conference on Cognitive Radio Oriented Wireless Networks and Communications in 2009, the IEEE Workshop on Cellular Cognitive Systems in 2014 and the IEEE Workshop Series on Mobile THz Systems started in 2018.